AVERAGED ROTATIONAL DYNAMICS OF GEO DEBRIS

C. J. Benson and D. J. Scheeres

University of Colorado, Boulder, CO, USA, Email: {conor.j.benson,scheeres}@colorado.edu

ABSTRACT

The growing number of defunct satellites in geosynchronous earth orbit (GEO) motivates continued development of active debris removal (ADR) and satellite servicing missions. These missions will benefit greatly from detailed target spin state information and accurate future predictions. The spin rates of defunct GEO satellites are diverse with uniform rotators and non-principal axis tumblers. For some satellites, observations show that these spin rates can change significantly over time including transitions between uniform rotation and tumbling. Modeling and observations have shown that some defunct GEO satellite spin states are largely driven by solar torques via the Yarkovsky-O'Keefe-Radzievskii-Paddack (YORP) effect. Recent studies of the tumbling YORP regime with full Euler dynamics models have uncovered dynamically rich behaviors that are consistent with satellite observations. Unfortunately, the full dynamics do not explain the fundamental mechanisms driving these behaviors. Furthermore, their computational overhead greatly hinders broad, long-term (i.e. multi-year) dynamical studies. To remedy these issues, we present tumbling averaged dynamics models that accurately capture and explain the behavior observed in the full dynamics while reducing computation times by up to three orders of magnitude. These averaged models promise to facilitate broad studies of long-term rotational dynamics for defunct satellites and rocket bodies.

Keywords: defunct satellites, rotational dynamics, solar torques, active debris removal, space situational awareness.

1. INTRODUCTION

To manage the growing space debris population and extend the operational life of aging satellites, a number of organizations are developing active debris removal (ADR) and satellite servicing missions. ADR/servicing spacecraft will need to rendezvous, grapple, and potentially de-spin large satellites not designed for such operations. As a result, accurate target spin state knowledge will be required to successfully execute these missions. ADR and servicing will be particularly important for geosynchronous earth orbit (GEO) where valuable longitude slots are limited and there are no natural de-orbit mechanisms to remove defunct satellites and other debris. Without remediation, debris populations in GEO and super-synchronous GEO graveyard orbits will continue to grow, posing increased collision risks to active spacecraft. Observations show that the spin rates of defunct GEO satellites are diverse and can change significantly over time [7, 9, 11, 15, 17]. Albuja et al. [1, 2] found that the rotational dynamics of some of these satellites are primarily driven by the Yarkovsky-O'Keefe-Radzievskii-Paddack (YORP) effect. The YORP effect is spin state evolution due to solar radiation and thermal re-emission torques [16]. Using a YORP dynamics model, Albuja et al. closely predicted the observed spin down of the defunct GEO satellite GOES 8 and its subsequent transition from uniform rotation to non-principal axis tumbling [1].

Further investigation of tumbling YORP for the defunct GOES satellites has uncovered rich dynamical behavior [4]. Simulations have shown tumbling cycles where the satellite transitions repeatedly between uniform rotation and tumbling due to YORP alone, spin-orbit coupling where the tumbling satellite's rotational angular momentum vector (pole) tracks and precesses about the sun/anti-sun direction, capture into tumbling period resonances where the satellite's attitude is periodic in time, and stable tumbling states when internal energy dissipation is considered. Recent radar and optical observations of the defunct GOES satellites show consistency with these simulated behaviors [3, 7, 8]. Light curves show that GOES 8 began spinning up after its transition to tumbling [7], consistent with YORP-driven tumbling cycles [4]. Doppler radar echoes for the tumbling GOES 8 and GOES 11 satellites collected at NASA Goldstone suggest their poles were near the sun or anti-sun directions in Feb. 2020 and Dec. 2019 respectively [3]. Radar and optical observations also strongly suggest GOES 8 was in a 5:1 tumbling period resonance in Feb. 2020 [3]. GOES 8 was likely in a tumbling resonance in Apr. 2018 as well [7]. Finally tumbling GOES 9 light curves collected in 2014 and 2016 show nearly identical structure [8], suggesting the satellite's tumbling state remained constant.

The above tumbling YORP simulations used Euler's equations of motion (i.e. the full dynamics). While these dynamics revealed a number of YORP-driven behaviors, they do not explain why the behaviors occur.

Also, these dynamics require short integration time-steps to accurately propagate the motion, especially for relatively rapid rotation, resulting in large computation times. This makes the full dynamics ill-suited for long-term (i.e. multi-year) simulations. In this paper, we outline alternative tumbling averaged dynamics models to understand the reasons for the observed behaviors and to enable fast exploration of long-term spin state evolution. More detailed derivation and exploration of these models can be found in Refs. [5] and [6], the former recently published and the latter currently in review. Our approach is analogous to orbit averaging, which has proven invaluable to studies of long-term orbital dynamics. In the remainder of the paper, we will first describe our slowly varying osculating elements and their equations of motion. We then discuss how these equations are averaged over the satellite's rotation. Summarizing results from Refs. [5] and [6], the averaged models are then validated against the full model and used to explore both general and resonant tumbling YORP. We finish by discussing implications of the results and providing conclusions.

2. DYNAMICS

The spin-orbit coupling observed in the full dynamics simulations motivates development of our averaged dynamics in the rotating sun-satellite frame. We make the reasonable assumption that the satellite directly orbits the sun in a circular orbit at earth's radial distance (i.e. 1 AU). This is valid because the satellite's GEO orbit is very small compared to the earth's orbit around the sun. We also neglect earth eclipses which are relatively infrequent and short-lived for GEO satellites, especially on the multi-year timescales considered. Figure 1 illustrates the rotating orbit frame used as the foundation of the averaged model. The $\hat{\boldsymbol{X}}$, $\hat{\boldsymbol{Y}}$, and $\hat{\boldsymbol{Z}}$ axes points along the ecliptic normal, orbital velocity, and sun directions respectively. Earth's heliocentric mean motion is denoted by n. Figure 1 also includes the satellite's rotational angular momentum frame with unit vectors $\hat{\boldsymbol{x}}$, $\hat{\boldsymbol{y}}$, and $\hat{\boldsymbol{z}}$ whose orientation with respect to the orbit frame is defined by the clocking angle α and coning angle β. Rotation from the orbit frame to angular momentum frame is given by a rotation about the $\hat{\boldsymbol{Z}}$ axis through α, followed by rotation about the $\hat{\boldsymbol{y}}$ axis through β. The $\hat{\boldsymbol{z}}$ axis is aligned with the rotational angular momentum vector $\boldsymbol{H}$. Rotation from the angular momentum frame to the satellite body-fixed frame is given by the (3-1-3) Euler angles ϕ, θ, and ψ [19].

The equations of motion for α, β, and the angular momentum magnitude $H = |\boldsymbol{H}|$ (see Ref. [5] for derivation) are given by,

$$\dot{\alpha} = \frac{M_y + Hn\cos\alpha\cos\beta}{H\sin\beta} \tag{1}$$

$$\dot{\beta} = \frac{M_x + Hn\sin\alpha}{H} \tag{2}$$

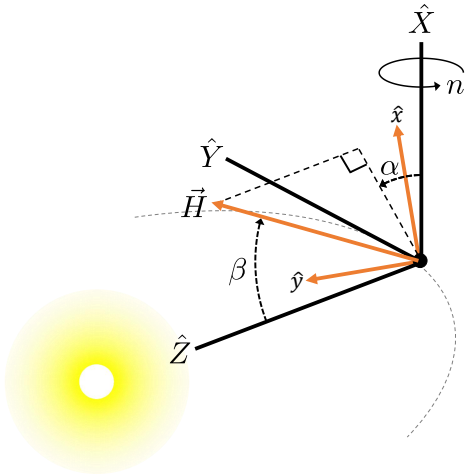

Figure 1: Orbit and angular momentum frames [5]

$$\dot{H} = M_z \tag{3}$$

where (M_x, M_y, M_z) denote the external torque components in the angular momentum frame.

An additional parameter is needed to describe the satellite's tumbling state. For this, we will use the dynamic moment of inertia I_d which defines the closed path that the satellite's angular velocity vector $\boldsymbol{\omega}$ takes through the body frame [12]. Mathematically, $I_d = H^2/2T$ where T is the rotational kinetic energy. I_d must lie between the satellite's minimum I_l and maximum I_s principal inertias because T is bounded for a given angular momentum. The equation of motion for I_d is given by,

$$\dot{I}_d = \frac{2I_d}{H}\boldsymbol{M}\cdot\left(I_{3\times3} - I_d[I]^{-1}\right)\hat{\boldsymbol{H}} \tag{4}$$

where $I_{3\times3}$ is the identity matrix and $[I]$ is the satellite's inertia tensor. We can define another fundamental parameter, the effective spin rate $\omega_e = H/I_d$.

For resonant tumbling, we must define an additional resonance angle γ that captures the phase offset between the two fundamental satellite motions. In torque-free rotation, a tumbling satellite's motion can be described by a pair of fundamental periods. $P_{\bar{\phi}}$ is the average precession period of the satellite's long axis about the angular momentum vector and P_ψ is the rotation period of the long axis about itself [18]. P_ψ is also the period of $\boldsymbol{\omega}$ in the body frame. The Euler angle ϕ is generally non-periodic and is driven on average by $P_{\bar{\phi}}$ whereas the θ and ψ motions are periodic in P_ψ and directly driven by the linearly scaled time parameter τ_r [5, 6, 18]. When $P_\psi/P_{\bar{\phi}} = m/n$ where m and n are positive, non-zero integers, the satellite is in a tumbling resonance. In such cases, the attitude motion approximately repeats with period $\Delta t = nP_\psi = mP_{\bar{\phi}}$. Taking $\dot{\varphi} = 2\pi/P_{\bar{\phi}}$ and $\dot{\tau}_r = 2\pi/P_\psi$, the equation of motion for γ is given by,

$$\ddot{\gamma} = n\ddot{\varphi} - m\ddot{\tau}_r \tag{5}$$

where $\ddot{\varphi}$ and $\ddot{\tau}_r$ are functions of the satellite inertias, I_d, $\dot{H}$, and $\dot{I}_d$ [6].

The multi-facet solar torque model used in this work is provided by Refs. [14, 20] and accounts for specular as well as Lambertian diffuse reflection and thermal re-emission. Thermal re-emission is assumed to be instantaneous. Also, self-shadowing and multi-bounce effects are neglected. The net force $\boldsymbol{f}_i$ on the ith facet is,

$$\boldsymbol{f}_i = -P_{SRP}\Big[\{\rho_i s_i(2\hat{\boldsymbol{n}}_i\hat{\boldsymbol{n}}_i - I_{3\times3}) + I_{3\times3}\}\cdot\hat{\boldsymbol{u}} + c_{di}\hat{\boldsymbol{n}}_i\Big]A_i\max(0,\hat{\boldsymbol{u}}\cdot\hat{\boldsymbol{n}}_i)$$

where P_{SRP} is the solar radiation pressure, ρ_i is the facet reflectivity, s_i is the specular fraction, $\hat{\boldsymbol{n}}_i$ is the facet unit normal vector, $\hat{\boldsymbol{u}}$ is the satellite to sun unit vector (aligned with $\hat{\boldsymbol{Z}}$), A_i is the facet area, and $c_{di} = B(1-s_i)\rho_i + B(1-\rho_i)$ where B is the scattering coefficient (2/3 for Lambertian reflection). The operation $\hat{\boldsymbol{n}}_i\hat{\boldsymbol{n}}_i$ represents a matrix outer product. The illumination function $\max(0,\hat{\boldsymbol{u}}\cdot\hat{\boldsymbol{n}}_i)$ ensures that facets do not contribute if the sun is below their local horizon.

The solar radiation torque acting on the faceted satellite model can then be calculated as,

$$\boldsymbol{M} = \sum_{i=1}^{n_f}\boldsymbol{r}_i \times \boldsymbol{f}_i \tag{6}$$

where $\boldsymbol{r}_i$ is the satellite center of mass to the facet centroid position vector and n_f is the number of facets.

The GOES 8 shape model illustrated in Figure 2 was used for all modeling assuming its known end of life mass properties and geometry as well as reasonable optical properties [5]. The principal axis body frame unit vectors $\hat{\boldsymbol{b}}_1$, $\hat{\boldsymbol{b}}_2$, and $\hat{\boldsymbol{b}}_3$ are labeled.

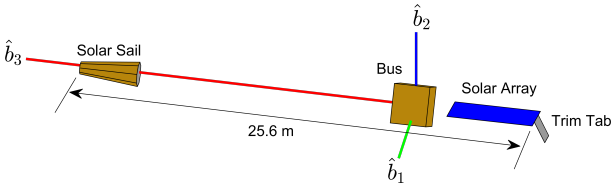

Figure 2: GOES 8 shape model [5]

3. AVERAGING

In order to average Eqs. 1 - 5, a few key assumptions are made. First, we assume that the solar torque is a small perturbation on the satellite's torque-free, rigid body rotation. We also assume that α, β, H, I_d, and γ change slowly compared to the satellite's attitude motion, defined by the (3-1-3) Euler angles ϕ, θ, and ψ. Note that γ only applies in the resonant case. We then average Eqs. 1 - 5 over the satellite's torque-free attitude motion [5, 18], holding α, β, H, I_d, and γ constant during this averaging process. This fundamentally requires averaging the solar torque components M_x, M_y, and M_z as well as $\dot{I}_d$.

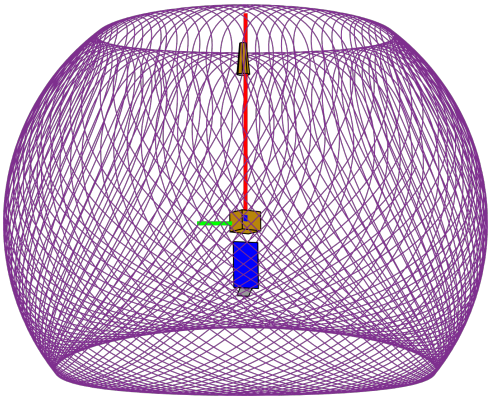

(a) Sun direction in body-fixed frame

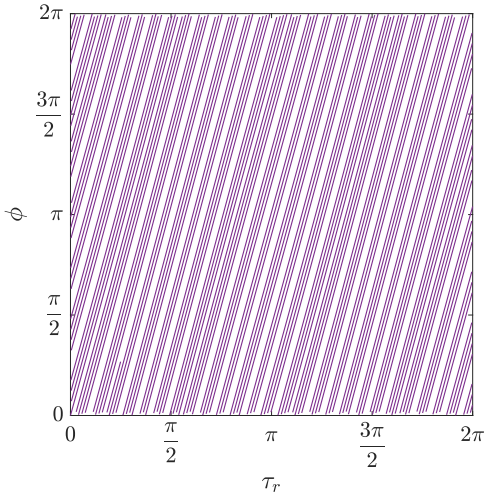

(b) Attitude in (τ_r, ϕ) angle space

Figure 3: Non-resonant motion

For the non-resonant case, $P_\psi/P_{\bar{\phi}}$ is irrational and the satellite's attitude motion is quasi-periodic (i.e. it does not exactly repeat). An example is provided in Figure 3. One could average Eqs. 1 - 4 over an arbitrarily long period of time so that the all possible attitudes are reached. This would be analogous to averaging over the path in Figure 3a. Nevertheless there is a more efficient approach that leverages the quasi-periodicity of the motion. In this non-resonant case, the ϕ and coupled (θ, ψ) motions are driven by different irrational frequencies. So we can average independently over these two motions. Considering Figure 3b, this is equivalent to taking an area average over the (τ_r, ϕ) angle space. Given the two irrational frequencies, the satellite attitude will approximately cover this area uniformly over time. With this approach, we convert an unbounded time average to a bounded area average. This area average can be conducted analytically or

numerically. Analytical averaging with the current solar torque model requires approximating the facet illumination function to make the integrals tractable [5]. This approximation reduces model accuracy to an extent but yields direct solutions for the averaged quantities $\overline{M_x}$, $\overline{M_y}$, $\overline{M_z}$, and $\dot{\bar{I}}_d$. Taking the numerical approach on the other hand, one simply samples M_x, M_y, M_z, and $\dot{I}_d$ on a uniform grid in (τ_r, ϕ) angle space and computes the average values. Note that this numerical approach does not require approximations to the solar torque model and allows for arbitrarily high fidelity formulations (e.g. ray-tracing), provided that thermal re-emission is considered instantaneous. For non-resonant averaging, $\overline{M_x}$, $\overline{M_y}$, $\overline{M_z}$, and the product $\dot{\bar{I}}_d\overline{H}$ are only functions of I_d and β for a given satellite. So for the numerical approach, 2D lookup tables can be pre-computed, using interpolation for simulation runs.

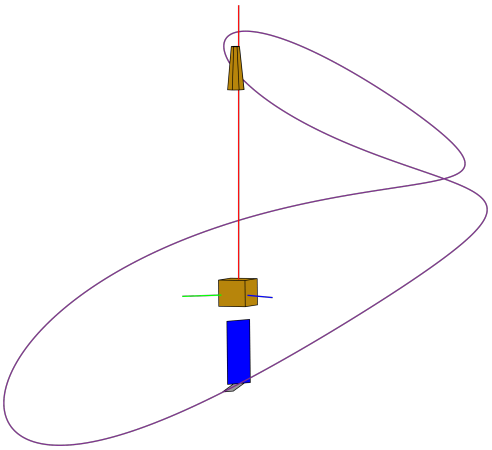

(a) Sun direction in body-fixed frame

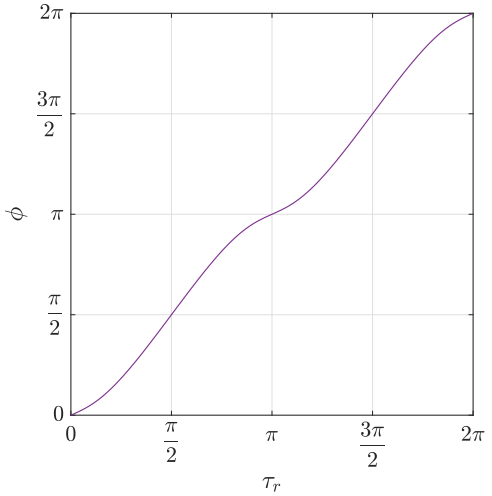

(b) Attitude in (τ_r,ϕ) angle space

Figure 4: Resonant motion with $P_\psi/P_{\bar{\phi}} = 1$

For the resonant case, the attitude motion is an approximately periodic trajectory. A representative example is shown in Figure 4 for the $P_\psi/P_{\bar{\phi}} = 1$ resonance. Here, we average over one cycle of this resonant motion. Different prescribed values for $\gamma = n\phi - m\tau_r$ will result in different relative phasing between τ_r and ϕ, thereby changing the shape of the trajectory in Figure 4a and shifting it up or down in Figure 4b. Taking the analytical averaging approach would require evaluating distinct sets of integrals for each resonance (i.e. each m, n combination). Instead, we numerically average the resonant trajectories over $\Delta t = nP_\psi = mP_{\bar{\phi}}$. For the resonant case, $\overline{M_x}$, $\overline{M_y}$, $\overline{M_z}$, and $\ddot{\bar{\gamma}}$ are only functions of γ and β.

With the averaging methodology now established, we can validate the resulting models against the full dynamics. Here, we generate the averaged quantities for both averaged models numerically. For the full dynamics, we use Euler's equations of motion and quaternions for our attitude coordinates [19]. Propagation is done with Matlab's ODE113 integrator with equal tolerances set for both the full and averaged models. For the first example, provided in Figure 5, we validate the general non-resonant tumbling averaged model. Starting both models with the provided initial conditions, we propagate the motion for three years. The satellite initially spins up and proceeds into more energetic tumbling. In Figure 5b, $I_d/I_s = 1$ denotes uniform rotation about the maximum inertia axis, the dashed grey line at $I_d/I_s = I_i/I_s$ denotes the separatrix between the short axis (SAM) and long axis (LAM) tumbling modes, and $I_d/I_s = I_l/I_s$ denotes uniform rotation about the minimum inertia axis. As the evolution proceeds, β gradually increases while α circulates rapidly. Once β passes through 90° (i.e. pole perpendicular to the sun direction), the satellite starts spinning down and returning towards uniform major axis rotation. For both models, the satellite then briefly spins up in uniform rotation with the pole moving rapidly towards the sun direction. The satellite then spins back down and transitions to tumbling where another cycle begins. Overall, the averaged model closely follows the full model evolution. Comparing simulation run times with 1e-12 relative and absolute tolerances, the full model required 70 min for this three year propagation while the averaged model only required 3 s. This is roughly a three order of magnitude decrease in computation time.

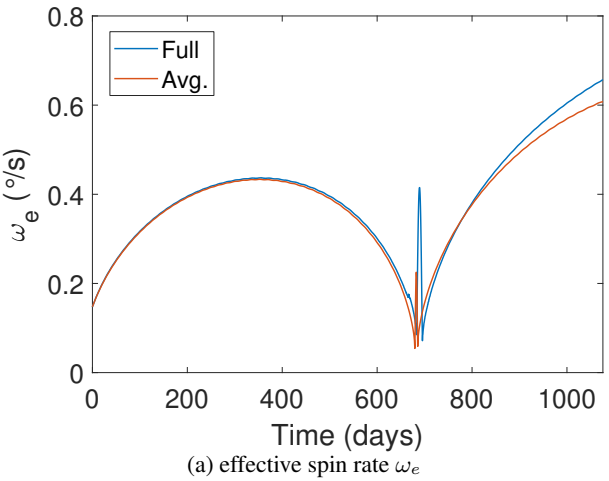

(a) effective spin rate ω_e

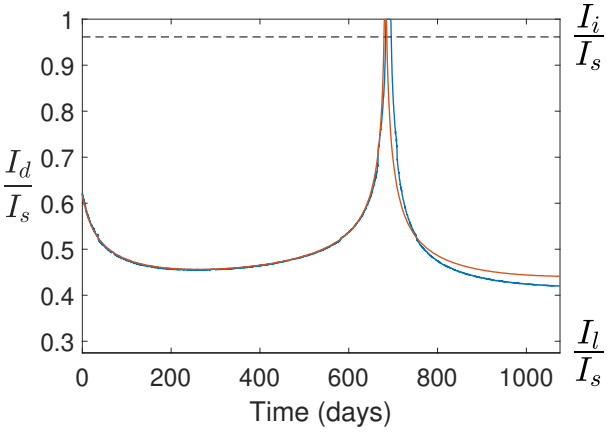

(b) normalized dynamic moment of inertia I_d/I_s

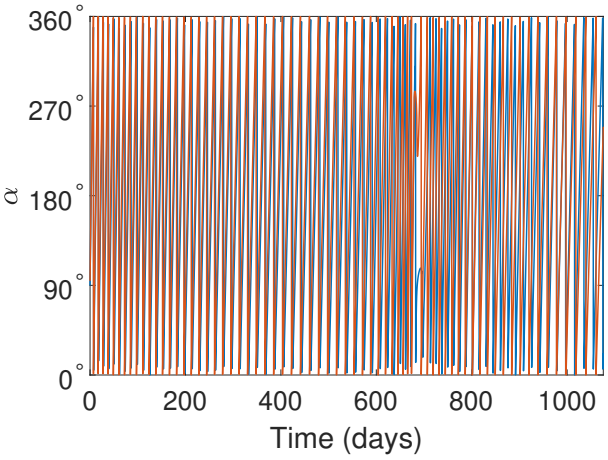

(c) clocking angle α

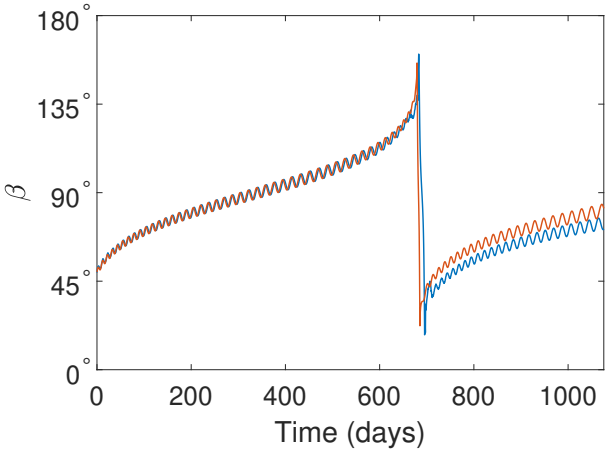

(d) coning angle β

Figure 5: Non-resonant averaged model validation ($\alpha_o = 95°$, $\beta_o = 50°$, $I_d/I_s = 0.62$, $2\pi/\omega_e = 40$ min)

Now we will validate the resonance averaged model against the full dynamics model for the $P_\psi/P_{\bar{\phi}} = 1$ resonance. For the full dynamics model, the initial resonance angle $\gamma_o = \phi_o - \tau_{r_o}$ is prescribed by setting $\tau_{r_o} = 0$ and solving for the corresponding ϕ_o. This is also how γ is defined for the averaged model [6]. Both models are propagated for 30 days with the initial conditions and resulting evolution provided in Figure 6. We see that the averaged model follows the full model closely initially, but the models begin to diverge as the simulation progresses particularly for γ and α. This is due in large part to our averaging assumption of holding I_d constant. Just off the resonance, the true trajectory becomes quasi-periodic which this averaged model does not consider. Nevertheless, the averaged model captures the general behavior of the full model. Also, in terms of run time for 1e-10 absolute and relative tolerances, the full model required roughly 27 s while averaged model required roughly 1 s.

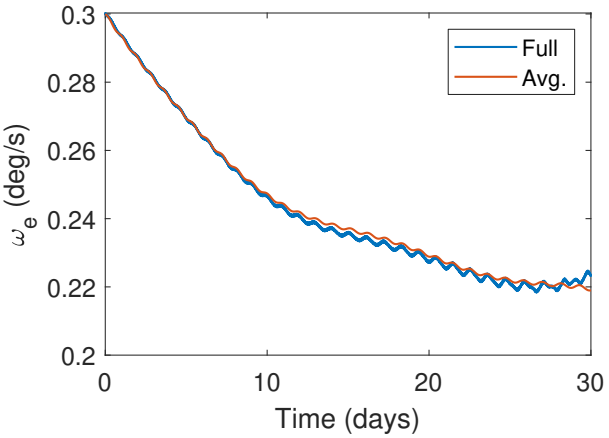

(a) effective spin rate ω_e

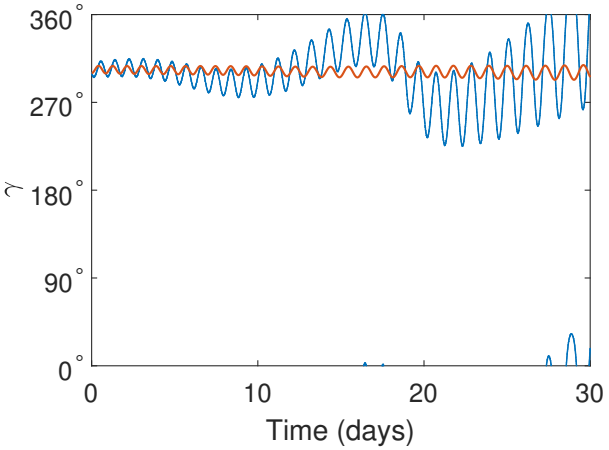

(b) normalized dynamic moment of inertia I_d/I_s

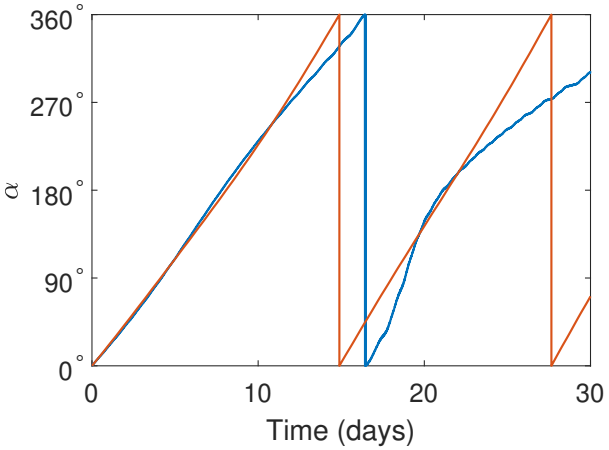

(c) clocking angle α

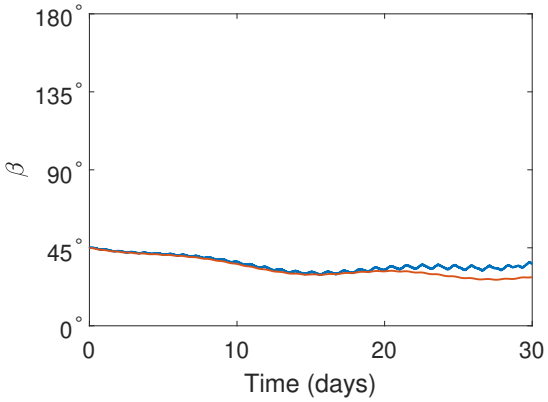

(d) coning angle β

Figure 6: Resonant averaged model validation ($\alpha_o = 0°$, $\beta_o = 45°$, $\gamma_o = 300°$, $2\pi/\omega_e = 20$ min) [6]

For a better overall comparison of the full and resonance averaged models, we can compare their resonance capture behavior. The satellite will remain captured in the resonance if γ oscillates about a fixed value and only escapes when γ begins circulating. For this analysis, we define escape when $|\gamma(t) - \gamma_o| > 6n\pi$, in other words when γ has progressed through three circulation cycles. Figure 7 shows the $P_\psi/P_{\bar{\phi}} = 1$ resonance capture contours for both models. Here, we simulate both models over a grid of (β_o, γ_o) values for 10 days. We see that the general capture behavior of the two models agrees well with slightly higher overall capture probability for the averaged model. Again, this is likely due to our fixed trajectory averaging approach which results in slightly greater stability. Interestingly, we see for extreme β values that capture does not occur for either model. There is also a gap along $\gamma_o \approx 160°$ where the satellite is not captured. This behavior will be explained in the following section.

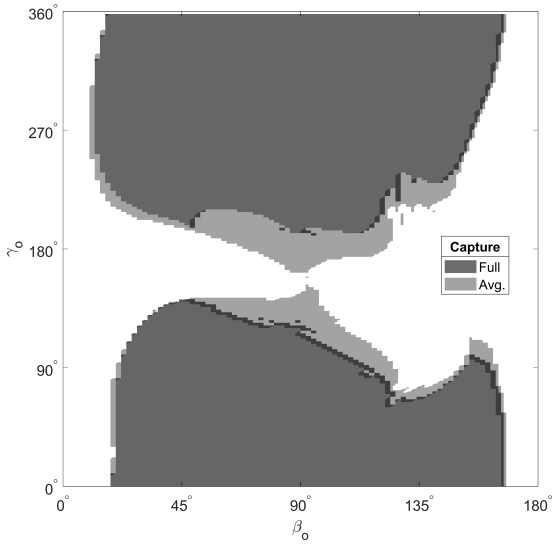

Figure 7: Full and averaged model capture in $P_\psi/P_{\bar{\phi}} = 1$ resonance for ≥10 days. White regions show escape. [6]

4. RESULTS

With the two averaged models validated, we can now use them to explain and efficiently explore the long-term tumbling behavior outlined in the introduction. First, we will investigate why we observe tumbling cycles in the full and averaged dynamics. Figure 8 shows the signs of the quantities $\dot{\bar{I}}_d$, $\dot{\bar{\beta}}$, and $\dot{\bar{\omega}}_e$ for GOES 8 with black regions denoting negative values and white denoting positive. Also included in Figure 8 is an averaged model run shown in red. Starting at the green dot, $\dot{\bar{I}}_d$ is negative which pushes the satellite across the separatrix (dashed line) and further into tumbling. Crossing the separatrix, $\dot{\bar{\beta}}$ switches from negative to positive, which pushes the satellite pole away from the sun. Also $\dot{\bar{\omega}}_e$ becomes positive, spinning the satellite up. This behavior continues until β passes roughly 90°. At this point, $\dot{\bar{I}}_d$ becomes positive and $\dot{\bar{\omega}}_e$ becomes negative. These combine to decelerate the satellite and push it back towards uniform rotation all while the pole continues moving away from the sun. Crossing the separatrix in the upward direction, $\dot{\bar{\beta}}$ becomes negative, pushing the pole back towards the sun. At this point, the satellite spin rate begins increasing as the satellite briefly returns to uniform rotation. When β decrease below 90°, $\dot{\bar{I}}_d$ becomes negative. This pushes the satellite back into tumbling where process repeats itself for the next tumbling cycle.

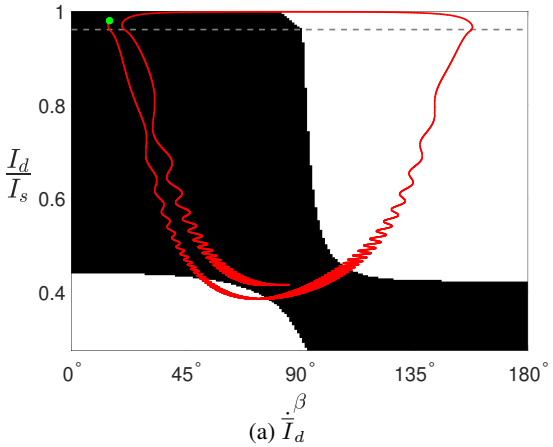

(a) $\dot{\bar{I}}_d$

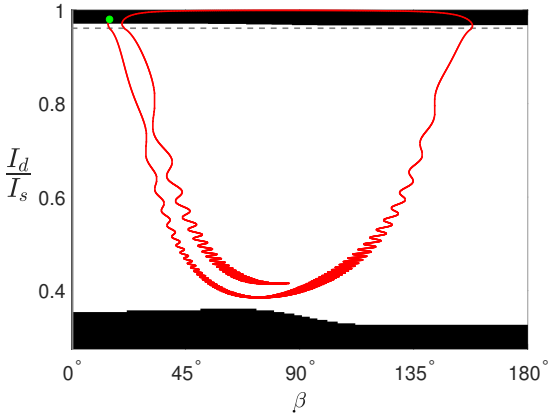

(b) $\dot{\bar{\beta}}$

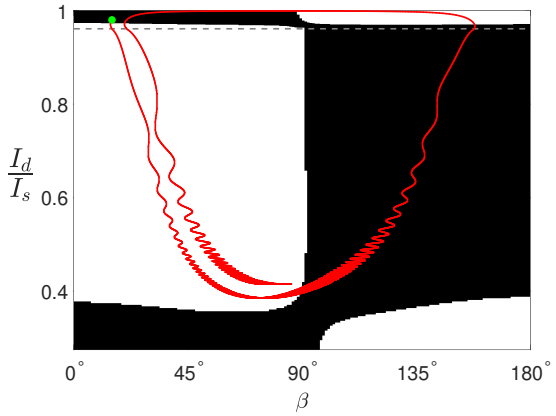

(c) $\dot{\overline{\omega}}_e$

Figure 8: Signs of GOES 8 averaged quantities with averaged model evolution overlaid. Black and white denote negative and positive values respectively. [5]

With the averaged models, we can also efficiently explore how the satellite's dynamical evolution could be affected by different end of life configurations. One significant degree of freedom is the final solar array angle. For the GOES 8-12 satellites, the solar array rotates once per day around the satellite's long axis ($\hat{\boldsymbol{b}}_3$ in Figure 2) axis to track the sun [21]. The final angles for these satellites differ because they were shut down at different local times [8]. These differing angles were found to significantly affect the satellite's long-term uniform spin state evolution [8]. With the current averaged models, we can readily extend that analysis to the tumbling regime. Figure 9 shows the relevant averaged quantities versus β and the end of life solar array angle θ_{sa} for the given SAM tumbling state. As we vary θ_{sa} (i.e. rotate the array around the $\hat{\boldsymbol{b}}_3$ axis), the averaged quantities change considerably, most notably $\overline{M_x}$, $\overline{M_z}$, and $\dot{\overline{I}}_d$. Furthermore, for GOES 8's particular end of life inertias and principal axes, $\overline{M_x}$, $\overline{M_z}$, and $\dot{\overline{I}}_d$ approach zero across almost all β values for θ_{sa} near odd multiples of 45°. This echoes the structure observed for the uniform spin averaged torques [8].

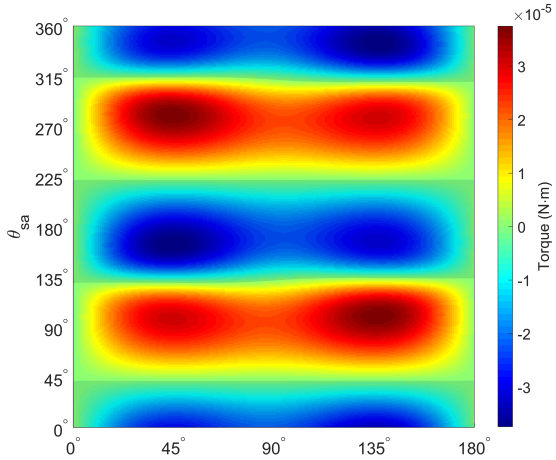

(a) $\overline{M_x}$

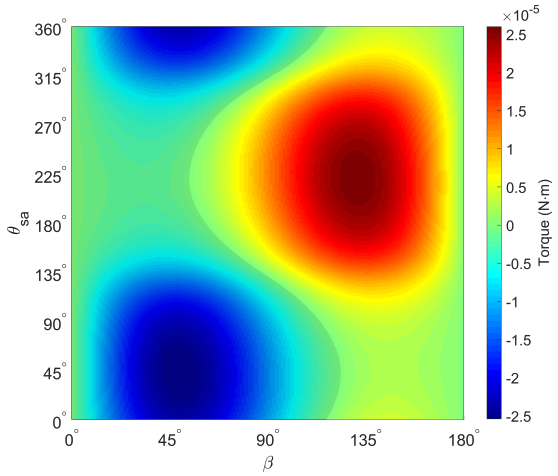

(b) $\overline{M_y}$

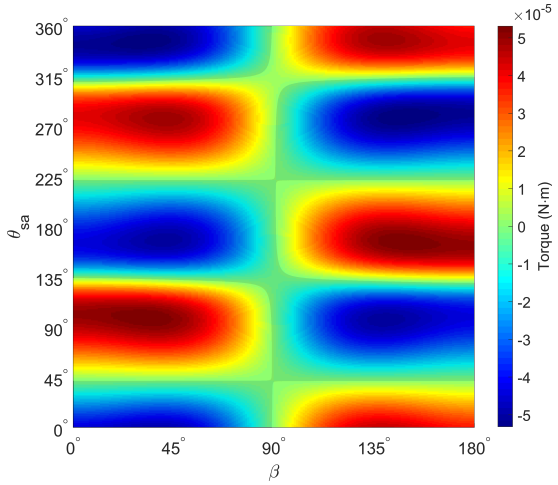

(c) $\overline{M_z}$

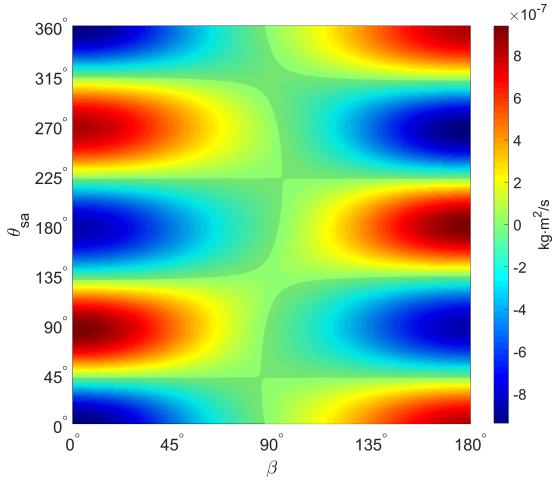

(d) $\dot{\overline{I}}_d$

Figure 9: GOES 8 averaged terms vs. β and end of life solar array angle θ_{sa} ($I_d/I_s = 0.98$) [5]

Another behavior discussed in the introduction was spin-orbit coupling with $\boldsymbol{H}$ tracking and precessing about the rotating sun direction. For GOES 8, we find that for the

majority of the tumbling regime, $|\overline{M_x}|, |\overline{M_z}|, << |\overline{M_y}|$ [5]. So the most of the torque goes into driving α. This is demonstrated by Figure 5c, where α circulates rapidly while the other parameters evolve much more slowly. Consulting Figure 1, $\hat{\boldsymbol{y}}$ is along the $\hat{\boldsymbol{Z}} \times \hat{\boldsymbol{H}}$ direction (i.e. perpendicular to both of these directions). So as $\hat{\boldsymbol{Z}}$ rotates in inertial space, $\hat{\boldsymbol{y}}$ follows. This tends to make $\hat{\boldsymbol{H}}$ move perpendicular to $\hat{\boldsymbol{Z}}$, resulting in sun-tracking precession.

In full model simulations, the satellite was often indefinitely captured in tumbling resonances due to YORP with $P_\psi/P_{\bar{\phi}} = 1{:}1$ and 2:1 being most common [5]. The resonance averaged model can help explain dynamical behavior in the vicinity of these resonances. Figure 10 shows $\ddot{\overline{\gamma}}$ for the 1:1 resonance. Also included are five averaged model trajectories. Note the $\ddot{\overline{\gamma}} = 0$ manifold running through the contour which separates the positive and negative regions. Considering cases 1 and 5 which have β values near 0° and 180°, $\ddot{\overline{\gamma}}$ does not change sign. So γ quickly decreases for case 1 and increases for case 5, resulting in circulation and escape from the resonance. For case 2, the satellite starts near the $\ddot{\overline{\gamma}} = 0$ manifold which in this region is stable because $d\ddot{\overline{\gamma}}/d\gamma$ is negative. So γ oscillates around the stable manifold and remains captured for an extended period of time. The behavior for case 3 is similar, only with larger oscillation amplitude due to the greater initial distance from the $\ddot{\overline{\gamma}} = 0$ manifold. Finally, for case 4, the satellite is initially placed near the unstable $\ddot{\overline{\gamma}} = 0$ manifold. Initially, $\ddot{\overline{\gamma}}$ is positive and γ increases. The solution then passes through the narrower $\ddot{\overline{\gamma}} < 0$ region, which cannot sufficiently slow γ. Given the vertical asymmetry between the positive and negative $\ddot{\overline{\gamma}}$ regions, γ continues increasing and begins circulating, causing the satellite to escape the resonance. Taken together, these cases help explain the resonance capture behavior observed in Figure 7. Escape is virtually guaranteed for extreme β values because the $\ddot{\overline{\gamma}} = 0$ manifold does not intersect these regions. Also, the horizontal escape region for $\gamma_o \approx 160°$ in Figure 7 is caused by proximity to the unstable $\ddot{\overline{\gamma}} = 0$ manifold.

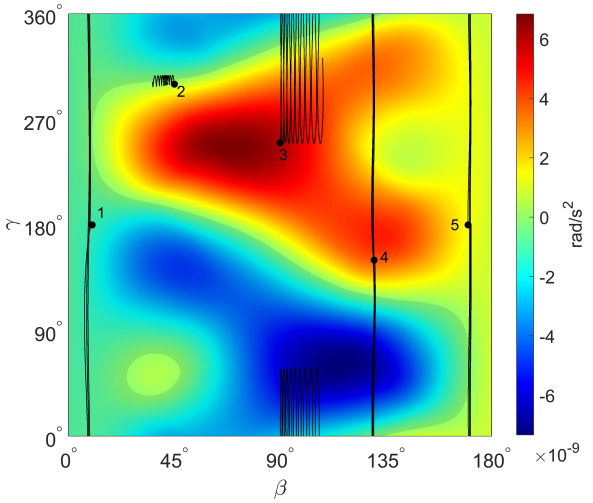

Figure 10: GOES 8 resonance-averaged $\ddot{\overline{\gamma}}$ contour with five overlaid runs ($P_\psi/P_{\bar{\phi}} = 1$). [6]

With indefinite resonance capture observed in full model results [5], determining the amount of time a satellite could remain captured is important. With the full model, this would be computationally expensive to investigate. Instead, we can use much faster resonance averaged model. Figure 11 shows the capture durations for the 1:1 resonance. Here, the averaged dynamics for each initial β_o and γ_o value were propagated until γ began circulating. The longest capture duration (∼283 days) occurs along the stable $\ddot{\overline{\gamma}} = 0$ manifold near case 2 in Figure 10.

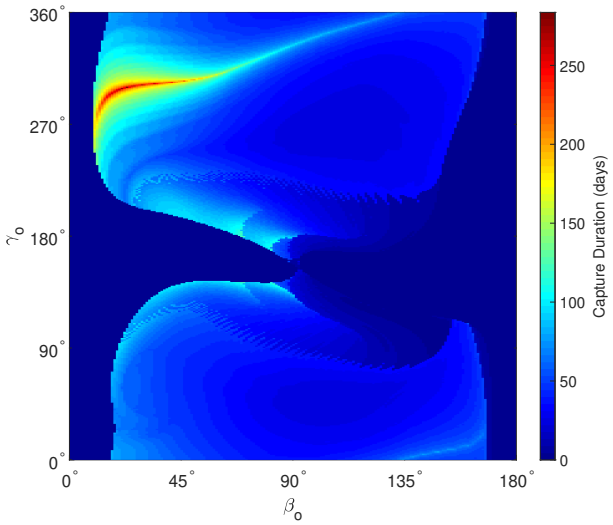

Figure 11: GOES 8 averaged resonance capture duration ($P_\psi/P_{\bar{\phi}} = 1$). [6]

For non-resonant tumbling states, γ rapidly circulates due to the irrationality of $P_\psi/P_{\bar{\phi}}$. So upon encountering a resonance, the initial γ value is essentially random. As a result, for a given β, the capture duration and spin state change a satellite will experience can be considered probabilistic. While only the 1:1 resonance was explored here, higher order resonances (e.g. 2:1, 3:2) can easily be studied [6].

5. DISCUSSION

The tumbling YORP dynamics explored above have a number of implications. First of all, the tumbling cycles observed in Figures 5 and 8 demonstrate the potential variability of defunct satellite spin states. For ADR and servicing, satellites in slow, uniform rotation will be easier to grapple and de-spin than those spinning rapidly. Similarly, slow rotation will reduce collision risk for the ADR/servicing spacecraft and save fuel and time required to de-spin. As a result, these missions will benefit greatly from accurate long-term spin state predictions to identify future windows where a target satellite is uniformly rotating as slowly as possible. Taking the simulation results above for example, one such window would be during the brief return to uniform rotation in

Figures 5 and 10. It would advantageous to let YORP decelerate target satellites as much as possible, saving the ADR/servicing spacecraft fuel and time. With numerous potential targets, one might plan to de-orbit the slowest spinning targets first, waiting for windows of predicted slow rotation to de-orbit others.

There is strong evidence that GOES 8 has been captured in a tumbling resonance at least once since 2018 [3, 4]. In these resonances, a satellite's attitude motion is nearly periodic. For general tumbling on the other hand, the attitude motion does not repeat. ADR/servicing spacecraft would have an easier time grappling a tumbling satellite with periodic rotation, especially if aiming for a particular feature on the satellite. For example, Northrop Grumman's Mission Extension Vehicle (MEV) docks with the apogee kick motor nozzle and concentric launch adapter ring commonly found on GEO satellites [10]. Taken together, the GOES 8 observations and potential advantage of resonant tumbling over general tumbling for ADR/servicing motivate further dynamical and observational studies to investigate whether these resonances are common among the tumbling defunct satellite population.

The results in Figure 9 suggest that the end of life solar array angle can greatly affect GOES 8's long-term spin state evolution. The significance of end of array angles for the GOES satellites is further supported by the dynamical and observational findings in Ref. [8]. This indicates that satellite designers and operators can potentially dictate post-disposal spin state evolution with factors other than the spin state at shutdown. For example, careful setting of end of life solar array angles could be used to reduce spin rates and spin rate variability, making future capture and de-orbit easier. Also, much of the high area-to-mass ratio (HAMR) debris near GEO is thought to be multi-layer insulation from defunct satellites and rocket bodies [13]. Reduced satellite spin rates may also reduce the formation rate of these HAMR objects.

6. CONCLUSIONS

In this paper, we outlined both resonant and non-resonant tumbling averaged rotational dynamical models and applied them to defunct GEO satellites subject to solar torques. These models capture the behavior of the corresponding full dynamics while reducing computation time by up to three orders of magnitude. More importantly, the averaged models clearly explain the behavior of the full model, enhancing understanding of long-term rotational dynamics. Overall, these averaged models promise to facilitate broad studies of defunct satellite and rocket body rotational dynamics to advance space situational awareness, active debris removal, and satellite servicing. While the current work was limited to solar torques, the averaged models can be readily extended to other perturbations such as internal energy dissipation and gravity gradient torques. These perturbations will be incorporated into future studies.

ACKNOWLEDGMENTS

This work was supported by a National Science Foundation (NSF) graduate research fellowship.

REFERENCES

1. A. Albuja, D. Scheeres, R. Cognion, W. Ryan, and E. Ryan. The YORP effect on the GOES 8 and GOES 10 satellites: A case study. *Advances in Space Research*, 61(1):122–144, 2018.
2. A. A. Albuja, D. J. Scheeres, and J. W. McMahon. Evolution of angular velocity for defunct satellites as a result of YORP: An initial study. *Advances in Space Research*, 56(2):237–251, 2015.
3. C. J. Benson, C. J. Naudet, D. J. Scheeres, et al. Radar and optical study of defunct geo satellites. *Proceedings of the Advanced Maui Optical and Space Surveillance Technologies Conference, Maui, HI*, 2020.
4. C. J. Benson and D. J. Scheeres. The YORP Effect for Tumbling Defunct GEO Satellites (AAS 19-858). *Proceedings of the AAS/AAIA Astrodynamics Specialist Conference, Portland, ME*, 2019.
5. C. J. Benson and D. J. Scheeres. Averaged solar torque rotational dynamics for defunct satellites. *Journal of Guidance, Control, and Dynamics*, 44(4), 2021.
6. C. J. Benson and D. J. Scheeres. Resonance-averaged solar torque dynamics for tumbling satellites. *Journal of Guidance, Control, and Dynamics*, in review.
7. C. J. Benson, D. J. Scheeres, W. H. Ryan, and E. V. Ryan. Cyclic complex spin state evolution of defunct GEO satellites. *Proceedings of the Advanced Maui Optical and Space Surveillance Technologies Conference, Maui, HI*, 2018.
8. C. J. Benson, D. J. Scheeres, W. H. Ryan, E. V. Ryan, and N. A. Moskovitz. GOES Spin State Diversity and the Implications for GEO Debris Mitigation. *Acta Astronautica*, 167:212–221, 2020.
9. R. L. Cognion. Rotation rates of inactive satellites near geosynchronous earth orbit. *Proceedings of the Advanced Maui Optical and Space Surveillance Technologies Conference, Maui, HI*, 2014.
10. V. Cox. Mission extension vehicle: Breathing life back into in-orbit satellites. `https://news.northropgrumman.com/news/features/mission-extension-vehicle-breathing-life-back-into-in-orbit-satellites`, retrieved Apr. 9, 2021.
11. M. A. Earl and G. A. Wade. Observations of the Spin-Period Variation of Inactive Box-Wing Geosynchronous Satellites. *Journal of Spacecraft and Rockets*, 52(3):968–977, 2015.

12. L. D. Landau and E. M. Lifshitz. *Mechanics*, volume 1. Pergamon Press, Oxford, England, 2nd edition, 1969, pp. 116-119.

13. J. C. Liou and J. K. Weaver. Orbital Dynamics of High Area-To Ratio Debris and Their Distribution in the Geosynchronous Region. *Proceedings of the 4th European Conference on Space Debris, Darmstadt. Germany*, 2005.

14. C. R. McInnes. *Solar Sailing: Technology, Dynamics and Mission Applications*. Springer-Praxis, Chichester, UK, 1st edition, 1999, ch. 2.

15. P. Papushev, Y. Karavaev, and M. Mishina. Investigations of the evolution of optical characteristics and dynamics of proper rotation of uncontrolled geostationary artificial satellites. *Advances in Space Research*, 43(9):1416–1422, 2009.

16. D. P. Rubincam. Radiative Spin-up and Spin-down of Small Asteroids. *Icarus*, 148(1):2–11, 2000.

17. W. H. Ryan and E. V. Ryan. Photometric Studies of Rapidly Spinning Decommissioned GEO Satellites. *Proceedings of the Advanced Maui Optical and Space Surveillance Technologies Conference, Maui, HI*, 2015.

18. N. H. Samarasinha and M. F. A'Hearn. Observational and Dynamical Constraints on the Rotation of Comet P/Halley. *Icarus*, 93(2):194–225, 1991.

19. H. Schaub and J. L. Junkins. *Analytical Mechanics of Space Systems*. American Insitute of Aeronautics and Astronautics, 3rd edition, 2014, pp. 11, 86-89, 110.

20. D. J. Scheeres. The dynamical evolution of uniformly rotating asteroids subject to YORP. *Icarus*, 188(2):430–450, 2007.

21. Space Systems/Loral. *GOES I-M Databook (Rev. 1)*. NASA, 1996. `https://goes.gsfc.nasa.gov/text/goes.databook.html`, retrieved Sept. 9, 2017.